Ionics (2016) 22:535–544
DOI 10.1007/s11581-015-1576-y

ORIGINAL PAPER

Fabrication of Ni-Co binary oxide/reduced graphene oxide composite with high capacitance and cyclicity as efficient electrode for supercapacitors

Yang Bai[1] · **Miaomiao Liu**[1] · **Jing Sun**[1] · **Lian Gao**[1]

Received: 17 March 2015 / Revised: 29 September 2015 / Accepted: 7 October 2015 / Published online: 24 October 2015

Abstract Nickel-cobalt binary oxide/reduced graphene oxide (G-NCO) composite with high capacitance is synthesized via a mild method for electrochemical capacitors. G-NCO takes advantages of reduced graphene oxide (RGO) and nickel-cobalt binary oxide. As an appropriate matrix, RGO is beneficial to form homogeneous structure and improve the electron transport ability. The binary oxide owns more active sites than those of nickel oxide and cobalt oxide to promote the redox reaction. Attributed to the well crystallinity, homogeneous structure, increased active sites, and improved charge transfer property, the G-NCO composite exhibits highly enhanced electrochemical performance compared with G-NiO and G-Co_3O_4 composites. The specific capacitance of the G-NCO composite is about 1750 F g^{-1} at 1 A g^{-1} together with capacitance retention of 79 % (900/1138 F g^{-1}) over 10,000 cycles at 4 A g^{-1}. To research its practical application, an asymmetric supercapacitor with G-NCO as positive electrode and activated carbon as negative electrode was fabricated. The asymmetric device exhibits a prominent energy density of 37.7 Wh kg^{-1} at a power density of 800 W kg^{-1}. The modified G-NCO composite shows great potential for high-capacity energy storage.

Keywords Supercapacitors · Ni-Co binary oxide · Reduced graphene oxide · High capacitance

Introduction

Electrochemical capacitors (ECs), as efficient energy storage devices, have been widely used in numerous fields such as hybrid electric vehicles (HEVs), mobile electronic devices, and military devices due to their ultra-high power density, long cycling stability, wide operation temperature range, and improved safety [1–3]. However, their low energy densities will restrict their practical applications. According to the formula $E=CU^2/2$, high capacitance (C) is beneficial to obtain high energy density (E). It is of technological importance to develop high capacitance electrode materials.

Transition metal oxides (TMOs), such as NiO, CoO, and Co_3O_4, are the typical electrode materials for ECs with high energy density. These materials show high theoretical specific capacitance due to their multiple oxidation states that result in a rich variety of redox reactions for pseudocapacitance generation [4–6]. However, one of the inevitable problems is that their practical capacitance values are still far lower than the theoretical ones, which can be attributed to the low activity of single component TMOs and its poor intrinsic electron transport ability. To solve these problems, two strategies are proposed. One is fabricating binary TMOs, which could exhibit superior properties over either of single component oxides [7–9]. The other is combining TMOs with electric matrix. Generally, the mixed valence state of binary metal ions will increase the active sites to trigger more redox reactions [10, 11], and different redox reactions can be successively conducted in the binary oxides. As a result, the binary oxides own enhanced capacitance and stability. Meanwhile, active

Electronic supplementary material The online version of this article (doi:10.1007/s11581-015-1576-y) contains supplementary material, which is available to authorized users.

✉ Jing Sun
jingsun@mail.sic.ac.cn

[1] The State Key Lab of High Performance Ceramics and Superfine Microstructure, Shanghai Institute of Ceramics, Chinese Academy of Sciences, 1295 Dingxi Road, Shanghai 200050, People's Republic of China

sites of different metal oxides can enlarge the voltage range of redox reaction. Kuang et al. synthesized hierarchical $NiCo_2O_4$ nanosheet-decorated Cu/CuO_x nanowire electrode, exhibiting the high specific capacitance of 578 F g^{-1}. The asymmetric device contained this electrode exhibited an energy density of 12.6 Wh kg^{-1} [12]. Wang et al. prepared Ni-Al-layered binary hydroxide with an enhanced capacitance of 795 F g^{-1} [13]. Chen et al. built binary nickel-cobalt hydroxide with a specific capacitance of 1000 F g^{-1} [14]. The capacitance and cyclicity of binary hydroxide were higher than those of $Ni(OH)_2$ or $Co(OH)_2$. These excellent researches verify the advantages of binary TMOs.

In the case of combining TMOs with matrix, the distribution of TMO particles can be more uniform. What's more, a matrix with good electron conductivity will remedy the bad intrinsic electron transport abilities of TMOs. The homogenous distribution enlarges the specific surface area to enhance the capacitance by increasing active sites. The improved electron transport property, meanwhile, results in enhanced cyclicity and rate capability. Among several matrix, carbon materials are one of the best choices due to their high specific surface area and excellent conductivity. Recently, reduced graphene oxide (RGO) is considered to be a component in EC composites investigated by some researchers [15–17] owing to its well electrical conductivity and high specific surface area and stability. Their results have shown that RGO as the matrix greatly benefits the capacitance. Huang et al. synthesized NiO nanoflakes/porous RGO composite to improve the capacitance (from 378 to 651 F g^{-1}) [18]. Xia et al. prepared $CoMoO_4$/RGO composites with higher specific capacitance (394 F g^{-1}), which was about 5.4 times of that of pure-$CoMoO_4$ [19]. When RGO acts as a two-dimensional matrix, not only the conductivity of composites is enhanced but the metal oxide particles are better distributed. Thus, more active sites can be involved in redox reaction to obtain high capacitance.

In this work, we proposed to synthesize a binary TMOs/RGO composite via a mild process. The precursor was prepared through a one-pot reaction, and the reagents used in this process were environmental friendly. Nickel oxide and cobalt oxide were chosen due to their adjacent reaction potential and high theoretical capacitance. Ni-Co binary oxide not only inherits the merits of both NiO and Co_3O_4 but also has hybrid architectures and superiority over single component oxides. Due to the synergistic effects of binary metal oxides and RGO, nickel-cobalt binary oxide/RGO (G-NCO) showed higher specific capacitance and cyclability than those of G-NiO and G-Co_3O_4. After 10,000 cycles at 4 A g^{-1}, G-NCO exhibits excellent cyclability with a capacitance retention of 79 %. The asymmetric device exhibited a prominent energy density of 37.7 Wh kg^{-1} at a power density of 800 W kg^{-1}, which makes G-NCO a promising material for electrode of ECs.

Experimental

Materials preparation

Graphite was purchased from Alfa Aesar (325 mesh). Nickel nitrate hexahydrate ($Ni(NO_3)_2{\cdot}6H_2O$, AR), cobalt nitrate hexahydrate ($Co(NO_3)_2{\cdot}6H_2O$, AR), urea (CON_2H_4, AR), and glucose (AR) were purchased from Shanghai Sinopharm Chemical Reagent Co., Ltd. (Shanghai, China). All chemicals were of analytic grade and used without further purification.

Graphene oxide (GO) was prepared from graphite flakes by a modified Hummers method [20, 21]. The as-prepared GO was dispersed in distilled water by ultrasonication, giving a yellow brown suspension with a concentration of 1 mg ml^{-1}.

Synthesis of nickel-cobalt binary oxide/RGO composite

Typically, 2 g glucose and 50 ml aqueous solution containing 1 mmol $Ni(NO_3)_2{\cdot}6H_2O$, 0.5 mmol $Co(NO_3)_2{\cdot}6H_2O$, and 1 g urea were slowly added into 108 ml GO suspension under stirring. Then, the mixture was refluxed at 95 °C for 12 h in an oil bath. The reaction product was filtrated and washed with distilled water and ethanol successively for several times, and finally dried and heated at 250 °C for 1.5 h in air. The obtained nickel-cobalt binary oxide/RGO composite powder was denoted as G-NCO. For comparison, NiO/RGO and Co_3O_4/RGO, denoted as G-NiO and G-Co_3O_4, respectively, were also prepared in the same route as G-NCO.

Characterization

The phase assemblage, chemical composition, and morphology of the powders were characterized by X-ray diffraction (XRD; Rigaku D/MAX-2200/PC with Cu Kα radiation), Raman spectroscopy (Thermo Scientific DXR Raman Microscope), X-ray photoelectron spectroscopy (XPS; VG Scientific 310F), field-emission scanning electron microscope (FE-SEM; Magellan Triton 400), and high-resolution transmission electron microscopy (HRTEM; JEOL JEM-2100F). The nitrogen adsorption isotherms of the powders were measured on MicroMeritics TriStar 3000 porosimeters at 77 K.

The electrochemical properties of the materials were characterized by three-electrode method in 2 M KOH aqueous solution at room temperature. The working electrode was prepared as follows. Active material, carbon black, and polyvinylidene fluoride (PVDF) binder in weight ratio of 80:10:10 was mixed in ethanol, and then pasted onto a nickel foam current collector (1 × 1 cm). Each working electrode was the same weight of 5 mg. A platinum wire was used as the

counter electrode and a saturate calomel electrode (SCE) as the reference electrode. The cyclic voltammetry (CV) at −0.1 to 0.5 V and the electrochemical impedance spectrum (EIS) applied an AC voltage with 5 mV amplitude in a frequency range from 0.01 to 100 kHz were measured on CHI660D Workstation (Shanghai, China). The galvanostatic charge and discharge tests were carried out in the potential range of 0 to 0.425 V on a LAND CT2001 battery tester. The specific capacitances C_s were calculated from the galvanostatic discharge curves using the equation [22]:

$$Cs = \frac{I \bullet t}{(\Delta V \bullet m)} \tag{1}$$

where I, t, ΔV, and m are the constant current (A), discharge time (s), total potential deviation (V), and mass of active materials (g), respectively.

An asymmetric supercapacitor was fabricated based on the G-NCO electrode as the positive electrode, the activated carbon (AC) electrode as the negative electrode, and polypropylene (PP) fiber as the separator. Particularly, the negative electrode was prepared as follows: AC, carbon black and PVDF binder in weight ratio of 80:10:10 was mixed in ethanol, and then pasted onto a nickel foam current collector (1×1 cm). The mass ratio of positive and negative electrodes was calculated by the charge balance theory ($q^+ = q^-$) [23]. In the relationship, the charge stored by each electrode usually depends on the specific capacitance (C), the potential window (Δv), and the mass of active material (m), as shown in Eq. 2:

$$q = C \times \Delta v \times m \tag{2}$$

In order to obtain $q^+ = q^-$, the mass balancing will be expressed as Eq. 3:

$$\frac{m_+}{m_-} = \frac{C_- \times \Delta v_-}{C_+ \times \Delta v_+} \tag{3}$$

Based on the specific capacitances of the G-NCO electrode and AC electrode, the optimal mass ratio between the two electrodes (m_+/m_-) was calculated to be about 0.295 in the asymmetric supercapacitor. The mass of AC is 13.55 mg. All the electrochemical experiments were carried out on a CHI660D workstation and LAND CT2001 battery tester in 2 M KOH electrolyte at room temperature. The energy density (E) and power density (P) of the asymmetric supercapacitor are estimated as follows [2]:

$$E \quad \frac{1}{2} C_s (\Delta v)^2 \tag{4}$$

$$P \quad \frac{E}{t} \tag{5}$$

where C_s (F g^{-1}) is the specific capacitance, t (s) is the discharge time, and Δv (V) is the potential change during the discharge process.

Results and discussion

G-NCO composite was prepared by a "controlled adsorption-nucleation-growth" process, as shown in Fig. 1. At room temperature, NH_4^+ was produced through urea hydrolysis, and it formed complexes with metal ions (Ni^{2+} and Co^{2+}). As a

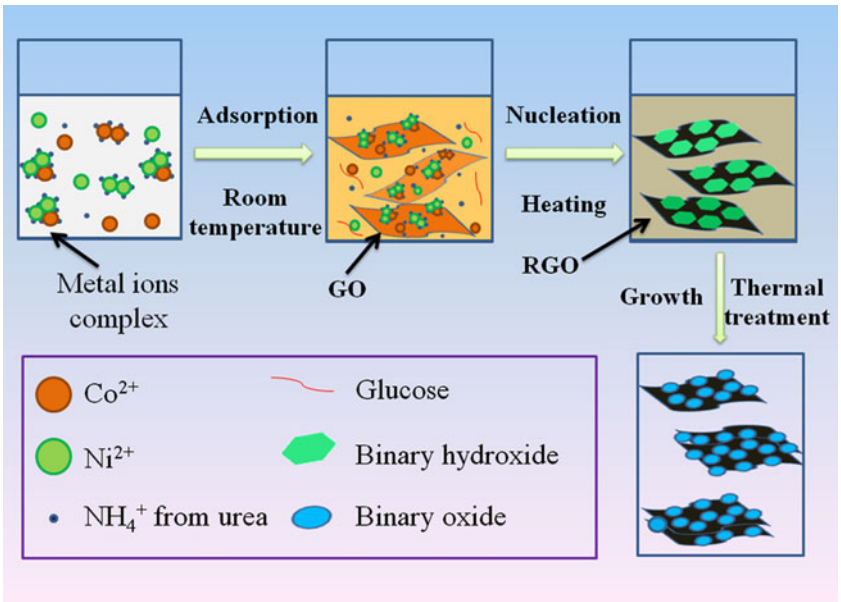

Fig. 1 The schematic illustration for the formation of G-NCO

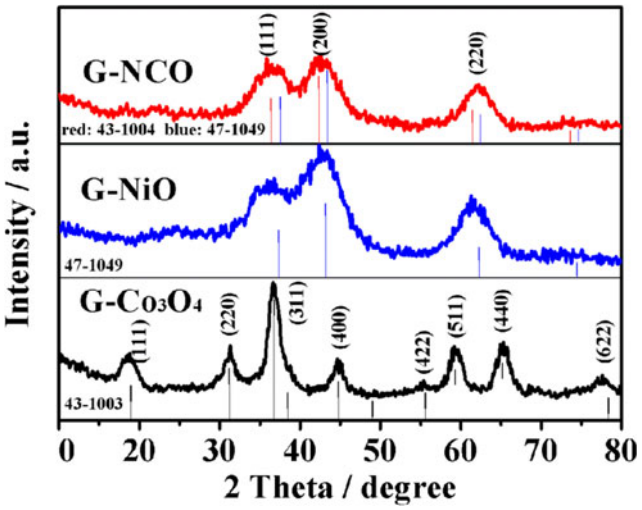

Fig. 2 XRD patterns of G-NiO, G-Co_3O_4, and G-NCO

result, the concentration of free metal ions in solution was decreased and accordingly, the growth rate of the crystals will be reduced [24–26]. When it was mixed with GO solution, the metal ions were attached onto negative-charged GO sheets due to electrostatic attraction effect (Table S1). Glucose played the role as a dispersing agent to stabilize GO suspension and make the metal ions distribute more uniformly [27], which has a positive effect on enhancing the crystallinity and cyclability of electrode materials (Fig. S1). At the heating stage, urea would provide OH^- ions through hydrolysis. And the released OH^- ions will be consumed by forming metal hydroxides with metal cations in the solution. According to chemical equilibrium, the reduction of OH^- concentration promotes urea hydrolysis. Then, urea will steadily supply OH^- ions for the nucleation and the formation of Ni-Co hydroxides (NCH) on GO surface. Meanwhile, GO was reduced to RGO by the combined effect of urea and glucose [27, 28]. After thermal treatment, the NCH/RGO composite (G-NCH) was transformed to G-NCO.

XRD were measured to confirm the crystal structure of products. For the GO sample (Fig. S2), a diffraction peak at 11.16° is consistent with (001) reflection, and after reduction, the characteristic peak of carbon from RGO could be found around 25.9° [29–31]. The XRD patterns of G-NiO, G-Co_3O_4, and G-NCO are displayed in Fig. 2. All of the samples show clear characteristic peaks of each metal oxide. Figure S1a confirms that glucose is beneficial to the good crystallinity, which plays the key role to guarantee the stability and capacity retention in the loop test [32]. The peaks of G-NiO and G-Co_3O_4 agree well with the standard diffraction card of face-centered-cubic NiO (JCPDS card no. 47-1049) and Co_3O_4 (JCPDS card no. 43-1003), respectively. This result demonstrates that nickel and cobalt atoms form different lattices when they have independent existences via our synthesis method. However, when both of nickel and cobalt atoms exist in the composite, no characteristic peaks of Co_3O_4 can be found. The characteristic peaks of NCO are consistent with both NiO and CoO (Fig. S2, no. 43-1004). It is well-known that NiO and CoO can form homogeneous solid solutions at all proportions in crystal structure, because they have very similar unit cell structures [33]. Considering the Ni/Co ratio was 2:1, NiO is believe to play a dominant role to form the lattice and a part of Ni sites are substituted by Co atoms. The ionic radius of Co is 74.5 pm, which is bigger than that of Ni (69 pm). The Co atoms enter into the lattice of NiO will lead the peak shift towards low angle (Table 1), demonstrating the formation of solid solution of (Ni, Co)O. Thus, both of Ni and Co atoms are expected to take part in the redox reaction to enhance the capacitance.

Table 1 2θ degrees of the standard NiO, CoO, and G-NCO

Peaks	(111)	(200)	(220)
NiO	37.248	43.275	62.878
CoO	36.503	42.401	61.520
G-NCO	36.733	42.724	62.140

Raman and XPS spectra were carried out on different samples to illustrate the reduction of GO. As exhibited in Fig. 3, distinctive D and G bands around 1350 and 1590 cm^{-1} are observed in all the four samples. The D band arises from the disorders and defects, while G band is caused by the vibration of sp^2-bonded carbon atoms in graphene [34, 35]. The intensity ratio of the D/G band (I_D/I_G) will increase when the structure defects increase. After the reduction process, I_D/I_G increases from 0.95 to ~1.10, which is consistent with the reported results [36, 37]. When GO is reduced to RGO, oxygen-containing functional groups are removed. Though the conjugated graphene network is reestablished, the size of the reestablished graphene network is usually smaller than the original graphene layer, resulting in the increase of I_D/I_G ratio

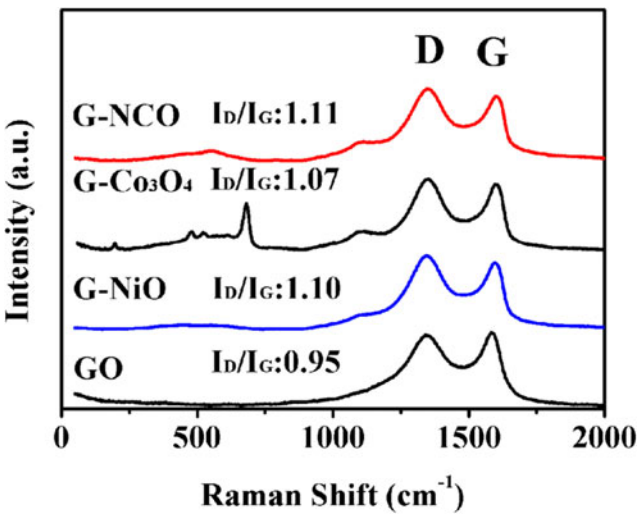

Fig. 3 Raman spectroscopy of GO, G-NiO, G-Co_3O_4, and G-NCO

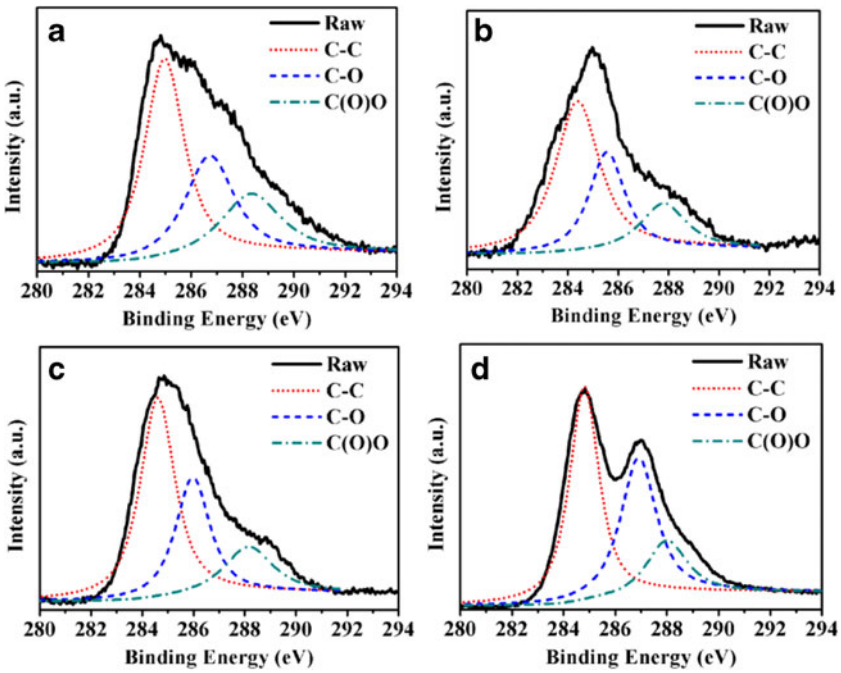

Fig. 4 The XPS spectrum of C1s for G-NiO **(a)**, G-Co_3O_4 **(b)**, G-NCO **(c)**, and GO **(d)**

[38]. Therefore, the increase of I_D/I_G ratio is reasonable after reduction. It is worthy to notice that the Raman spectrum of G-Co_3O_4 shows three peaks at 500, 740, and 1100 cm^{-1}. While, the peak at 740 cm^{-1} disappears in G-NCO, illustrating that the lattice of cobalt oxide has changed. This phenomenon is in consistence with the XRD results. High-resolution C1s XPS spectra of G-NiO (panel a), G-Co_3O_4 (panel b), G-NCO (panel c), and GO (panel d) are exhibited in Fig. 4. The absorbance band intensities of carbonyl carbon (C–O) and carboxylate carbon (O–C=O, C(O)O) in GO are much higher in comparison with their counterparts in the other three samples. The ratios of non-oxygenated (C–C), C–O, and C(O)O are calculated in Table S2. The decrease of the C–O and C(O)O ratios and increase of C–C ratios in G-NiO, G-Co_3O_4, and G-NCO illustrates that the oxygen-containing functional groups are removed via the reduction process. Less oxygen-containing functional groups in RGO lead to improved conductivity. The higher conductivity of RGO is more suitable for electron transport and consequently to enhance the rate capability and cyclicity. The Ni 2p and Co 2p spectra both shows two spin-orbit doublets with shakeup satellites peaks (Fig. S3), which illustrates that the NCO in G-NCO is a composition of Ni^{2+}, Ni^{3+}, Co^{2+}, and Co^{3+}. The Ni/Co ratio of G-NCO is 2.3:1, corresponding to the reactant ratio.

To characterize the morphology and fine structure of products, SEM and HRTEM images were observed. SEM images of G-NiO, G-Co_3O_4, and G-NCO were exhibited in Fig. 5. All of the samples show the wrinkle of RGO. The TMO particles are too small to be observed. However, the EDS mappings confirm that the distribution of Ni or Co in each composite is uniform over all composites. TEM images display the surface information and the morphology of metal oxide particles. As shown in Fig. 6a, GO is clearly observed with a seriously folded structure, which is induced by intermolecular π-π stacking interaction to minimize the internal energy of the system. The paper-like GO sheets are suitable to act as substrates to grow and anchor functional nanoparticles. For G-NiO, G-Co_3O_4, and G-NCO samples, all the metal oxide particles exhibit good dispersion on RGO (Fig. S4). This structure is suitable for active materials contacting with electrolyte, contributing to increase more active sites to conduct more redox reactions. Figure 6b shows the particles of G-NiO with the size of below 2 nm uniformly attach on RGO sheets. In G-Co_3O_4 samples (Fig. 6c), similar homogeneously distribution

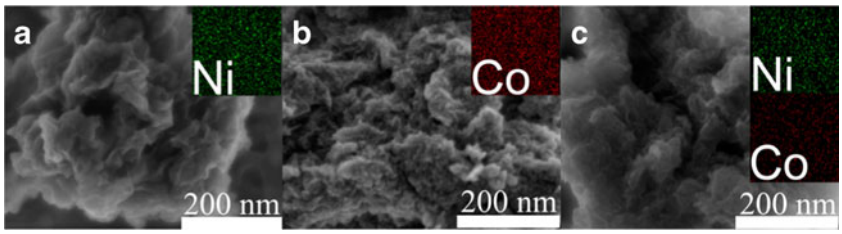

Fig. 5 SEM images of G-NiO **(a)**, G-Co_3O_4 **(b)**, and G-NCO **(c)**; the *insets* show the element (Ni or Co) mapping of these samples, respectively

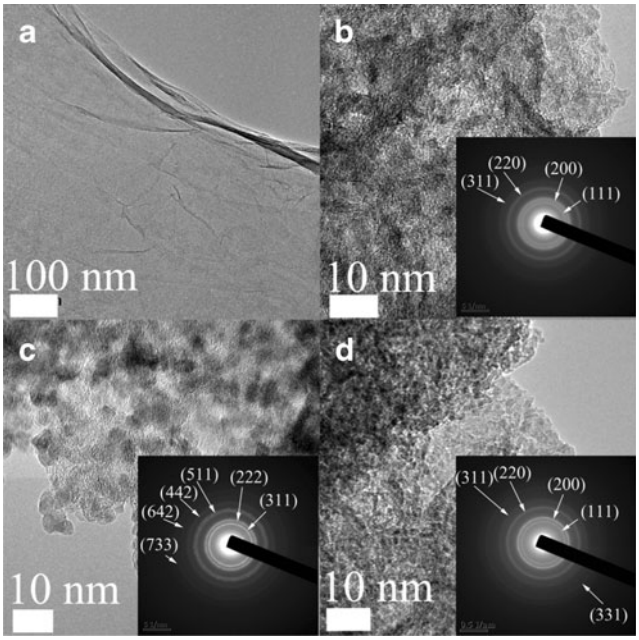

Fig. 6 TEM images of GO **(a)**, G-NiO **(b)**, G-Co_3O_4 **(c)**, and G-NCO **(d)**

of nanoparticles on RGO sheets can be observed, but the particle size is much larger than that of NiO. These particles with size of 6–8 nm exhibit clear lattice fringes, demonstrating better crystallinity. In Fig. 6d, NCO particles can be found clearly covering almost all the surface of RGO. The particle size is about 4 nm, which is affected by the coexistence of Ni and Co ions and between the particle sizes of NiO and Co_3O_4 in G-NiO and G-Co_3O_4. The select area electron diffraction (SAED) also demonstrates that the composites are polycrystalline with cubic structure. G-Co_3O_4 shows different diffraction rings with G-NiO and G-NCO, meaning that Co ions have changed its lattice when it combines with NiO. The definition of the diffraction rings also illustrated that the crystallinity of G-NCO composite is higher than that of NiO, corresponding with the XRD results.

Apart from the morphology, the specific surface area (SSA) and pore size distribution also have an important effect on electrochemical performance. The SSAs of G-NiO (panel a), G-Co_3O_4 (panel b), and G-NCO (panel c) were measured by nitrogen adsorption/desorption measurement (Fig. 7). All the samples exhibit typical Langmuir type IV characteristics with obvious hysteresis loops, indicating that the samples contain a certain amount of mesoporous [39]. The hysteresis loops of G-NiO (Fig. 7a) and G-NCO (Fig. 7c) is H1 type, illustrating the uniform distribution and relative small size of pores. Contrary to them, the H3 type loop of G-Co_3O_4 (Fig. 7b) suggests that certain aggregation happens among the particles. The SSA calculated by the BET method and the average pore size are listed in Table 2. As the SSA is one of the most important properties that we are concerned and its value is closely dependent on the particle size, it is clear that G-NCO is satisfying due to its large SSA value (450.6 $m^2\ g^{-1}$) and corresponding small particle size. Large SSA can provide more active sites for redox reaction, which leads to high capacitance. Another important factor for redox reaction is the pore size. G-NiO and G-NCO both show one pore size distribution (the inset of Fig. 7a, b). The average pore size is 3.8 and 3.9 nm, respectively, which just falls within the appropriate pore size range of 2–5 nm for supercapacitors [40, 41]. Although G-Co_3O_4 has an average pore size of 3.7 nm, its wide pore size distribution and low SSA make it hard to perform high capacitance (the inset of Fig. 7c). Considering all the above analysis, G-NCO owns well crystallinity, large SSA, suitable pore size,

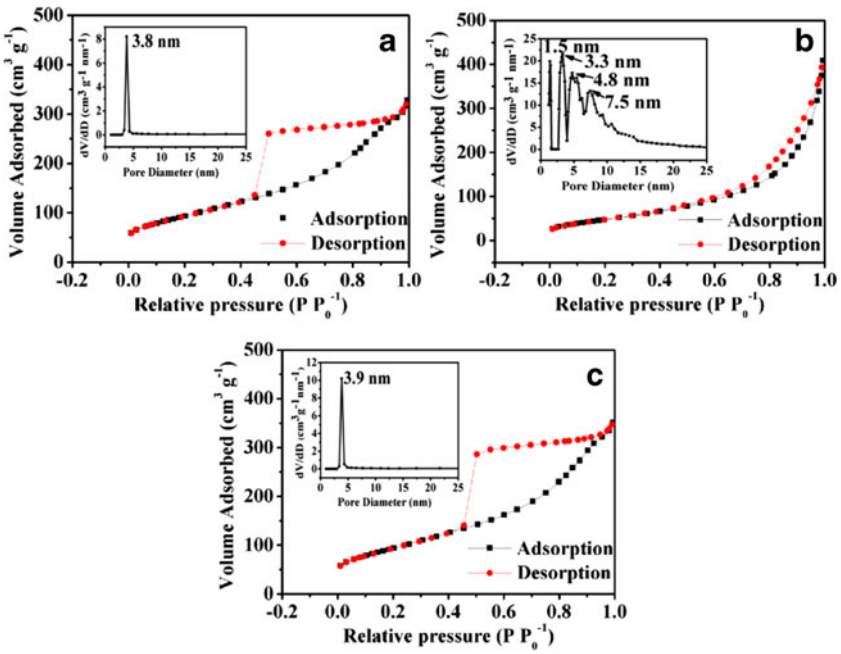

Fig. 7 N_2 adsorption-desorption isotherms of G-NiO **(a)**, G-Co_3O_4 **(b)**, and G-NCO **(c)**; the *inset* is the BJH pore size distribution on the basis of the desorption branch

Table 2 The values of specific surface area and pore size on the basis of the desorption branch of G-NiO, G-Co_3O_4, and G-NCO

	G-NiO	G-Co_3O_4	G-NCO
Specific surface area/m^2 g^{-1}	471.5	246.1	450.6
Average pore size/nm	3.8	3.7	3.9

and expected conductivity. What's more, coexistence of Ni and Co atoms increases more active sites for redox reaction. Thus, excellent capacitance, cyclicity, and stability will be obtained when it acted as an electrode for supercapacitor.

In order to further certify the superiority of G-NCO as an electrode for ECs, electrochemical performances of G-Co_3O_4, G-NiO, and G-NCO were measured by using CV and galvanostatic curves. Figure 8a shows the CV curves at 5 mV s^{-1}. Each electrode shows a pair of obvious redox peaks, corresponding to the reversible redox reaction related to M-O/M-O-OH, where *M* represents Ni or Co ions [42, 43]. According to the equation for specific capacitance ($C=\int IdV/2\Delta vs$), a larger area surrounded by the CV curve relates to a higher specific capacitance. The CV curve of G-NCO shows the largest surrounding area, illustrating the enhanced specific capacitance and electrochemical reactivity. The peaks are broader than those of G-Co_3O_4 and G-NiO, which means that the active sites are increased and both of Ni and Co ions take part in the redox reaction. The anodic and cathodic peaks of G-NCO are shifted towards the negative potential due to the reaction of both Ni and Co ions [44, 45]. As seen from Fig. 8b, all the samples show typical pseudo-capacitive behavior with highly nonlinear discharge curves, which is consistent with the CV curves. It is worthy to notice that the discharge curve of G-NCO exhibits two inflections, which are consistent with the two reactions of NiO and CoO. It is believed that the discharge time is controlled by the rate of alkali ions diffusing into and out of the surface of the electrode [16]. And the longer discharge time is, the higher the capacitance is. The longest discharge time of G-NCO illustrates the highest capacitance, which is attributed to increased redox reactions caused by uniform structure, large SSA, and great activity caused by the coexistence of Ni and Co atoms. To further analyze the electrochemical performance of G-Co_3O_4, G-NiO, and G-NCO electrodes, different current densities are applied (Fig. 8c). Under the same conditions, the specific capacitance of the G-NCO electrode is much higher than those of G-NiO and G-Co_3O_4 electrodes. Through calculation, the specific capacitances at 1 A g^{-1} are 877,555 and 1750 F g^{-1} for G-NiO, G-Co_3O_4, and G-NCO, respectively. The high capacitance of G-NCO is higher than those of similar systems in reported literatures [11, 46]. Generally, capacitance decreases with the increase of the current density. The specific capacitances of G-NiO and G-Co_3O_4 drops to 715 and 489 F g^{-1} at 4 A g^{-1}, respectively, while the specific capacitance of G-NCO still remains 1138 F g^{-1} at the same current density. Even at high current density of 10 A g^{-1}, the specific capacitance of G-NCO is still as high as 776 F g^{-1}, which is much higher than those of G-NiO (564 F g^{-1}) and G-Co_3O_4 (423 F g^{-1}). Fig. 8d displays the cyclability of G-NiO, G-Co_3O_4, and G-NCO electrodes at 4 A g^{-1}. The capacity retention ratios of G-Co_3O_4, G-NiO, and G-NCO are 87, 73, and 79 % over 10,000 cycles, respectively. The capacitance of G-NCO is still as high as 900 F g^{-1}. The high capacitance and stability make it a promising material for ECs.

To better understand the advantage of G-NCO, the electrodes were subjected to AC impedance measurements. Electrochemical impedance spectroscopy was measured to

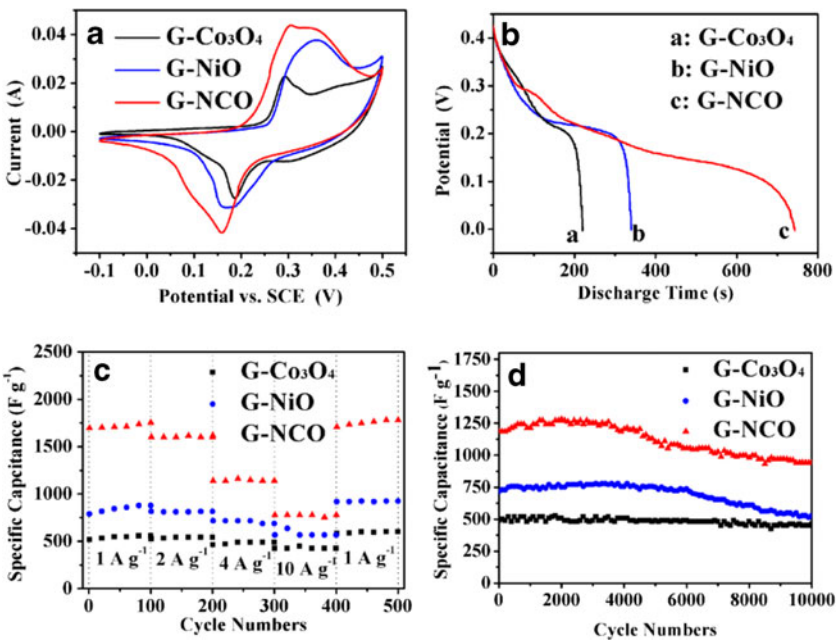

Fig. 8 **a** CV curves of G-Co_3O_4, G-NiO, and G-NCO electrodes at a scan rate of 5 mV s^{-1}. **b** The galvanostatic discharge curves of G-Co_3O_4, G-NiO, and G-NCO electrodes at 1 A g^{-1}. **c** Rate capacitance of G-Co_3O_4, G-NiO, and G-NCO electrodes with increasing current densities. **d** Cyclic performance of G-Co_3O_4, G-NiO, and G-NCO electrodes at 4 A g^{-1}

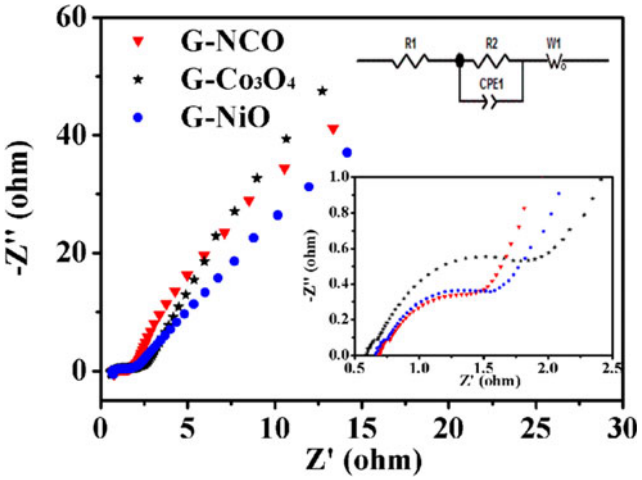

Fig. 9 Electrochemical impedance spectra (*EIS*) obtained from G-NiO, G-Co_3O_4, and G-NCO electrodes. The *inset* shows the enlarged EIS of the electrodes and the equivalent circuit diagram

analyze the electron transport properties of these samples. Figure 9 shows the Nyquist plots of G-NiO, G-Co_3O_4, and G-NCO electrodes. It is well accepted that the intercept at the real part (Z_{re}) is the total ESR, which is a combination of the electrolyte resistance, contact resistance at interface, and the intrinsic resistance of the electrode [5, 43]. The ESRs obtained by complex non-linear leasts square (CNLS) fitting were around 0.66, 0.60, and 0.69 Ω for G-NiO, G-Co_3O_4, and G-NCO, respectively. The values are small and similar, indicating that all of these electrodes have superior electrical conductivity. All of the spectra display depressed semicircles in high-frequency region and straight lines in low-frequency region. The semicircle is related with the charge transfer resistance, which is determined by the surface area and electrical conductivity [47, 48]. Through fitting, the charge transfer resistances (R_{ct}) were 1.357, 1.971, and 1.298 Ω for G-NiO, G-Co_3O_4, and G-NCO, respectively. G-NCO shows the smallest semicircle and the lowest charge transfer resistance in these three electrodes because of the high SSA and the superiority of Ni-Co binary oxides. It is reported that the substitution of cobalt compounds into nickel systems can contribute to enhance the electrochemical performance by improving the active site density, conductivity, and roughness [49–51]. In the low-frequency region, the straight line reflects the diffusion of the electro-active species [52]. The nearly vertical line indicates rapid ion diffusion in the electrolyte and adsorption onto the electrode surface [15]. The G-NCO electrode shows the largest slope, demonstrating that binary system is suitable to the rapid ion diffusion. It is concluded that G-NCO favored the charge transfer and ion diffusion due to improved electrical conductivity and increased tunnels caused by RGO and the coexistence of Ni and Co atoms.

Based on above analysis, G-NCO exhibits an excellent high capacitance, well-cyclability, and high capacity retention, which is expected to be a promising electrode material of ECs. The following factors are believed to be possible for the excellent electrochemical performance: firstly, Ni-Co binary oxide inherits the merits of both NiO and CoO and has superiority over single component oxides. Due to the atom substitution, G-NCO owns more active sites for redox reaction to enhance the capacitance. Secondly, RGO has positive effects on the capacitance and cyclicity when it acts as a matrix. The functional groups on the RGO surface can anchor NCO nanoparticles to form a homogeneous structure, leading to a high

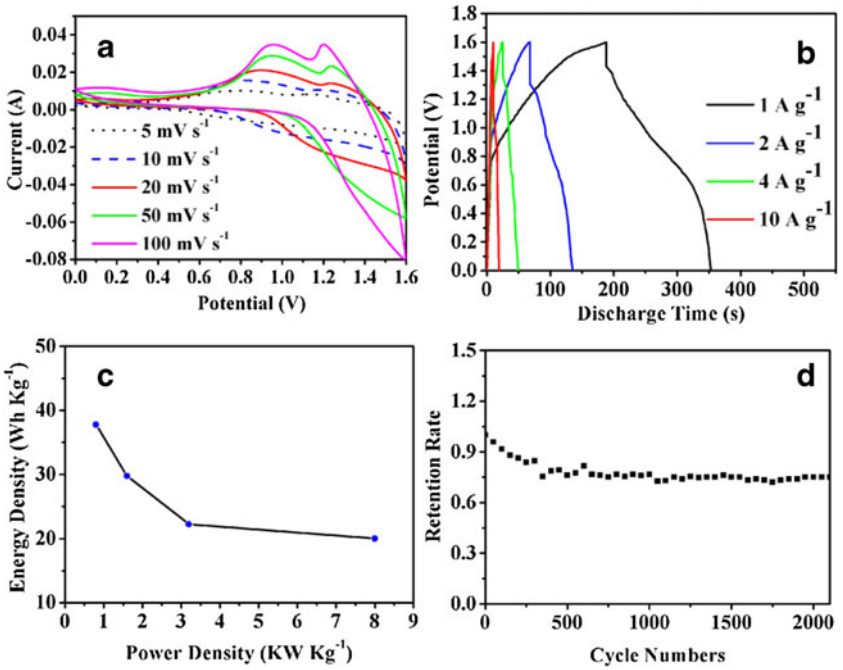

Fig. 10 Electrochemical performance of the asymmetric supercapacitor measured in 2 M KOH electrolyte. **a** CV curves at different scan rates, **b** discharge profiles at different current densities, **c** Ragone plot related to energy and power densities, and **d** cycling stability at 4 A g^{-1}

specific surface area. It will make active material contact with electrolyte more efficient and sufficient, and then more redox reaction would be reacted. RGO also could make up the poor intrinsic conductivity of metal oxide due to its well electron transport ability. The well crystallinity, homogeneous structure, increased active sites, and improved charge transfer property contribute to a significant improvement in capacitive and cycling performance of the G-NCO electrode.

An asymmetric supercapacitor has been fabricated to further illustrate the potential application of the G-NCO composite. Figure 10a exhibits the typical CV curves of the asymmetric supercapacitor at different scan rates, which shows collective contribution of electric double-layer capacitance and pseudocapacitance at 0–1.6 V. With the scan rate increasing from 5 to 100 mV s^{-1}, the CV curves retain similar shapes, indicating high fast charge-discharge properties of the device [53]. At different current densities, symmetric triangular-shaped charge and discharge curves could be clearly observed, suggesting a rapid I-V response (Fig. 10b). At 1, 2, 4, and 10 A g^{-1}, the specific capacitances are 106, 84, 63, and 56 F g^{-1}, respectively. The capacitance retention is 53 % when the current density increases from 1 to 10 A g^{-1}. As shown in the Ragone plot (Fig. 10c), a high energy density of 37.7 Wh kg^{-1} at the power density of 800 W kg^{-1} and a high power density of 8000 W kg^{-1} was obtained at the energy density of 20 Wh kg^{-1} was achieved. The maximum energy density of our asymmetric supercapacitor is higher than those of the devices in reported literatures (<25 Wh kg^{-1}) [11, 53, 54]. The durability of the as-fabricated asymmetric supercapacitor is also evaluated. As displayed in Fig. 10d, the capacitance retention rate is 75 % of its original capacitance after 2000 cycles. The above performance makes the G-NCO electrode promising as an attractive candidate for energy storage.

Conclusion

In summary, we successfully synthesized nickel-cobalt binary oxide/RGO (G-NCO) composite with high capacitance for energy storage via a mild method. Ni-Co binary oxide has superiority over single component oxides. More active sites and decreased charge transfer resistance compared with those of NiO and Co_3O_4 will be obtained. RGO is a good choice for the matrix to anchor nanoparticles. The particle size could also be adjusted, and the particles are uniformly attached on the RGO surface. Taking the advantages of the above factors, G-NCO shows high specific capacitance and better cyclicity and stability than those of G-NiO and G-Co_3O_4. Additionally, the as-fabricated asymmetric supercapacitor delivers a prominent energy density of 37.7 Wh kg^{-1}. The high capacitance makes G-NCO appropriate to be electrode material for electrochemical capacitor with high energy density.

Acknowledgments This work is supported by the National Basic Research Program of China (2012CB932303) and the National Natural Science Foundation of China (grant no. 51072215 and 51172261).

References

1. Yu L, Zhang GQ, Yuan CZ, Lou XW (2013) Hierarchical NiCo2O4@MnO2 core-shell heterostructured nanowire arrays on Ni foam as high-performance supercapacitor electrodes. Chem Commun 49(2):137–139
2. Chen H, Hu LF, Chen M, Yan Y, Wu LM (2014) Nickel-cobalt layered double hydroxide nanosheets for high-performance supercapacitor electrode materials. Adv Funct Mater 24(7):934–942
3. Chang J, Jin M, Yao F, Kim TH, Le VT, Yue H, Gunes F, Li B, Ghosh A, Xie S, Lee YH (2013) Asymmetric supercapacitors based on graphene/MnO2Nanospheres and graphene/MoO3Nanosheets with high energy density. Adv Funct Mater 23(40):5074–5083
4. Lu ZY, Yang Q, Zhu W, Chang Z, Liu JF, Sun XM, Evans DG, Duan X (2012) Hierarchical Co3O4@Ni-Co-O supercapacitor electrodes with ultrahigh specific capacitance per area. Nano Res 5(5):369–378
5. Wang GX, Cai J, Xu HF, Lu L, Zhao H (2014) Enhanced capacitance of a NiO electrode prepared in the magnetic field. J Appl Electrochem 44(3):391–398
6. Xu H, Zhuang JX, Li JL, Zhang JL, Lu HL (2014) Liquid precipitation synthesis of Co3O4 for highperformance electrochemical capacitors. Ionics 20(4):489–494
7. Wang GP, Liu LX, Zhang L, Zhang JJ (2013) Nickel, cobalt, and manganese oxide composite as an electrode material for electrochemical supercapacitors. Ionics 19(4):689–695
8. Yang F, Yao J, Liu F, He H, Zhou M, Xiao P, Zhang Y (2013) Ni–Co oxides nanowire arrays grown on ordered TiO2 nanotubes with high performance in supercapacitors. J Mater Chem A 1(3):594
9. Kuang M, Wen ZQ, Guo XL, Zhang SM, Zhang YX (2014) Engineering firecracker-like betamanganese dioxides@spinel nickel cobaltates nanostructures for high-performance supercapacitors. J Power Sources 270:426–433
10. Kang JL, Hirata A, Qiu HJ, Chen LY, Ge XB, Fujita T, Chen MW (2014) Self-grown Oxy-Hydroxide@ nanoporous metal electrode for high-performance supercapacitors. Adv Mater 26(2):269–272
11. Wang H, Holt CMB, Li Z, Tan X, Amirkhiz BS, Xu Z, Olsen BC, Stephenson T, Mitlin D (2012) Graphene-nickel cobaltite nanocomposite asymmetrical supercapacitor with commercial level mass loading. Nano Res 5(9):605–617
12. Kuang M, Zhang YX, Li TT, Li KF, Zhang SM, Li G, Zhang W (2015) Tunable synthesis of hierarchical NiCo2O4 nanosheets-decorated Cu/CuOx nanowires architectures for asymmetric electrochemical capacitors. J Power Sources 283:270–278
13. Wang B, Liu Q, Qian Z, Zhang X, Wang J, Li Z, Yan H, Gao Z, Zhao F, Liu L (2014) Two steps in situ structure fabrication of Ni–Al layered double hydroxide on Ni foam and its electrochemical performance for supercapacitors. J Power Sources 246:747–753
14. Chen J-C, Hsu C-T, Hu C-C (2014) Superior capacitive performances of binary nickel–cobalt hydroxide nanonetwork prepared by cathodic deposition. J Power Sources 253:205–213
15. Kim M, Hwang Y, Kim J (2013) Graphene/MnO2-based composites reduced via different chemical agents for supercapacitors. J Power Sources 239:225–233
16. Zhu X, Dai H, Hu J, Ding L, Jiang L (2012) Reduced graphene oxide–nickel oxide composite as high performance electrode materials for supercapacitors. J Power Sources 203:243–249

17. Sheng Chen JZ, Xiaodong W, Qiaofeng H, Xin W (2010) Graphene oxide MnO2 nanocomposites for supercapacitors.pdf. ACS Nano 4:2822–2830
18. Huang ML, Gu CD, Ge X, Wang XL, Tu JP (2014) NiO nanoflakes grown on porous graphene frameworks as advanced electrochemical pseudocapacitor materials. J Power Sources 259:98–105
19. Xia X, Lei W, Hao Q, Wang W, Wang X (2013) One-step synthesis of CoMoO4/graphene composites with enhanced electrochemical properties for supercapacitors. Electrochim Acta 99:253–261
20. Hummers WS Jr, Offeman RE (1958) Preparation of Graphitic Oxide. J Am Chem Soc 80:1339
21. Yu Z, McInnis M, Calderon J, Seal S, Zhai L, Thomas J (2015) Functionalized graphene aerogel composites for high-performance asymmetric supercapacitors. Nano Energy 11:611–620
22. Xia XH, Tu JP, Mai YJ, Chen R, Wang XL, Gu CD, Zhao XB (2011) Graphene sheet/porous NiO hybrid film for supercapacitor applications. Chem Eur J 17(39):10898–10905
23. Yan J, Fan ZJ, Sun W, Ning GQ, Wei T, Zhang Q, Zhang RF, Zhi LJ, Wei F (2012) Advanced asymmetric supercapacitors based on Ni(OH)2/graphene and porous graphene electrodes with high energy density. Adv Funct Mater 22(12):2632–2641
24. Gao H, Wang G, Yang M, Tan L, Yu J (2012) Novel tunable hierarchical Ni-Co hydroxide and oxide assembled from two-wheeled units. Nanotechnology 23(1):015607
25. Song YC, Wang J, Li ZS, Guan DH, Mann T, Liu Q, Zhang ML, Liu LH (2012) Self-assembled hierarchical porous layered double hydroxides by solvothermal method and their application for capacitors. Microporous Mesoporous Mater 148(1):159–165
26. Yuan CZ, Zhang XG, Su LH, Gao B, Shen LF (2009) Facile synthesis and self-assembly of hierarchical porous NiO nano/micro spherical superstructures for high performance supercapacitors. J Mater Chem 19(32):5772–5777
27. Zhu CZ, Guo SJ, Fang YX, Dong SJ (2010) Reducing sugar: new functional molecules for the green synthesis of graphene nanosheets. ACS Nano 4(4):2429–2437
28. Zhao B, Song J, Liu P, Xu W, Fang T, Jiao Z, Zhang H, Jiang Y (2011) Monolayer graphene/NiO nanosheets with two-dimension structure for supercapacitors. J Mater Chem 21(46):18792–18798
29. Li B, Cao H, Yin J, Wu YA, Warner JH (2012) Synthesis and separation of dyes via Ni@reduced graphene oxide nanostructures. J Mater Chem 22(5):1876
30. Gao Z, Wang J, Li Z, Yang W, Wang B, Hou M, He Y, Liu Q, Mann T, Yang P, Zhang M, Liu L (2011) Graphene nanosheet/Ni2+/Al3+ layered double-hydroxide composite as a novel electrode for a supercapacitor. Chem Mater 23(15):3509–3516
31. Xu Y, Sheng K, Li C, Shi G (2010) Self-assembled graphene hydrogel via a one-step hydrothermal process. ACS Nano 4(7):4324–4330
32. Mao L, Zhang K, Chan HSO, Wu JS (2012) Nanostructured MnO2/graphene composites for supercapacitor electrodes: the effect of morphology, crystallinity and composition. J Mater Chem 22(5):1845–1851
33. Kuboon S, Hu YH (2011) Study of NiO-CoO and Co3O4-Ni3O4 solid solutions in multiphase Ni-Co-O systems. Ind Eng Chem Res 50(4):2015–2020
34. Su CY, Xu YP, Zhang WJ, Zhao JW, Tang XH, Tsai CH, Li LJ (2009) Electrical and spectroscopic characterizations of ultra-large reduced graphene oxide monolayers. Chem Mater 21(23):5674–5680
35. Casiraghi C, Ferrari AC, Robertson J (2005) Raman spectroscopy of hydrogenated amorphous carbons. Phys Rev B 72(8):085401
36. Sobon G, Sotor J, Jagiello J, Kozinski R, Zdrojek M, Holdynski M, Paletko P, Boguslawski J, Lipinska L, Abramski KM (2012) Graphene oxide vs. reduced graphene oxide as saturable absorbers for Er-doped passively mode-locked fiber laser. Opt Express 20(17):19463–19473
37. Kim S, Ku SH, Lim SY, Kim JH, Park CB (2011) Graphene-biomineral hybrid materials. Adv Mater 23(17):2009–2014
38. Ji ZY, Shen XP, Zhu GX, Zhou H, Yuan AH (2012) Reduced graphene oxide/nickel nanocomposites: facile synthesis, magnetic and catalytic properties. J Mater Chem 22(8):3471–3477
39. Zhong-Shuai Wu WR, Da-Wei W, Feng L, Bilu L, Hui-Ming C (2010) High-energy MnO2 NanowireGraphene and graphene asymmetric electrochemical capacitors.pdf. ACS Nano 4:5835–5842
40. Wang L, Liu XH, Wang X, Yang XJ, Lu LD (2010) Preparation and electrochemical properties of mesoporous Co3O4 crater-like microspheres as supercapacitor electrode materials. Curr Appl Phys 10(6):1422–1426
41. Zhou HS, Li DL, Hibino M, Honma I (2005) A self-ordered, crystalline-glass, mesoporous nanocomposite for use as a lithium-based storage device with both high power and high energy densities. Angew Chem Int Ed 44(5):797–802
42. Lu ZY, Zhu W, Lei XD, Williams GR, O'Hare D, Chang Z, Sun XM, Duan X (2012) High pseudocapacitive cobalt carbonate hydroxide films derived from CoAl layered double hydroxides. Nanoscale 4(12):3640–3643
43. Sun X, Wang GK, Hwang JY, Lian J (2011) Porous nickel oxide nano-sheets for high performance pseudocapacitance materials. J Mater Chem 21(41):16581–16588
44. Wang Y-M, Zhang X, Guo C-Y, Zhao Y-Q, Xu C-L, Li H-L (2013) Controllable synthesis of 3D NiχCo1–χ oxides with different morphologies for high-capacity supercapacitors. J Mater Chem A 1(42):13290
45. Kong L, Deng L, Lang J, Ji X, Luo Y, Kang L (2012) Enhanced electrochemical capacitive properties of nickel-cobalt oxide nanoflakes materials. Chin J Chem 30(3):570–576
46. Wang X, Liu WS, Lu X, Lee PS (2012) Dodecyl sulfate-induced fast faradic process in nickel cobalt oxide–reduced graphite oxide composite material and its application for asymmetric supercapacitor device. J Mater Chem 22(43):23114
47. Hu CC, Chen WC, Chang KH (2004) How to achieve maximum utilization of hydrous ruthenium oxide for supercapacitors. J Electrochem Soc 151(2):A281–A290
48. Zhang YX, Kuang M, Hao XD, Liu Y, Huang M, Guo XL, Yan J, Han GQ, Li J (2014) Rational design of hierarchically porous birnessite-type manganese dioxides nanosheets on different onedimensional titania-based nanowires for high performance supercapacitors. J Power Sources 270:675–683
49. Zhong JH, Wang AL, Li GR, Wang JW, Ou YN, Tong YX (2012) Co3O4/Ni(OH)(2) composite mesoporous nanosheet networks as a promising electrode for supercapacitor applications. J Mater Chem 22(12):5656–5665
50. Chen J, Bradhurst DH, Dou SX, Liu HK (1999) Nickel hydroxide as an active material for the positive electrode in rechargeable alkaline batteries. J Electrochem Soc 146(10):3606–3612
51. Li Y, Hasin P, Wu Y (2010) NixCo3–xO4 nanowire arrays for electrocatalytic oxygen evolution. Adv Mater 22(17):1926–1929
52. Wang L, Dong ZH, Wang ZG, Zhang FX, Jin J (2013) Layered α-Co(OH)2Nanocones as electrode materials for pseudocapacitors: understanding the effect of interlayer space on electrochemical activity. Adv Funct Mater 23(21):2758–2764
53. Wang X, Sumboja A, Lin M, Yan J, Lee PS (2012) Enhancing electrochemical reaction sites in nickelcobalt layered double hydroxides on zinc tin oxide nanowires: a hybrid material for an asymmetric supercapacitor device. Nanoscale 4(22):7266–7272
54. Tang C, Tang Z, Gong H (2012) Hierarchically porous Ni-Co oxide for high reversibility asymmetric full-cell supercapacitors. J Electrochem Soc 159(5):A651–A656